Monthly Notices of the ROYAL ASTRONOMICAL SOCIETY

MNRAS **503,** 614–624 (2021) doi:10.1093/mnras/stab475
Advance Access publication 2021 February 19

Fast infrared variability from the black hole candidate MAXI J1535−571 and tight constraints on the modelling

F. M. Vincentelli [1]★ P. Casella,[2] D. M. Russell [3] M. C. Baglio,[3] A. Veledina [4,5,6] T. Maccarone,[7] J. Malzac,[8] R. Fender,[9] K. O'Brien[10] and P. Uttley[11]

[1]*Department of Physics and Astronomy, University of Southampton, Southampton SO17 1BJ, UK*
[2]*INAF, Osservatorio Astronomico di Roma Via Frascati 33, I-00078 Monteporzio Catone, Italy*
[3]*Center for Astro, Particle and Planetary Physics, New York University Abu Dhabi, PO Box 129188, Abu Dhabi, UAE*
[4]*Department of Physics and Astronomy, FI-20014 University of Turku, Finland*
[5]*Nordita, KTH Royal Institute of Technology and Stockholm University, Roslagstullsbacken 23, SE-10691 Stockholm, Sweden*
[6]*Space Research Institute of the Russian Academy of Sciences, Profsoyuznaya Str. 84/32, Moscow 117997, Russia*
[7]*Texas Tech University, Physics and Astronomy Department, Box 41051, Lubbock, TX 79409-1051, USA*
[8]*IRAP, Universite' de Toulouse, CNRS, UPS, CNES, Toulouse, France*
[9]*Department of Physics, Astrophysics, University of Oxford, Denys Wilkinson Building, Keble Road, Oxford, OX1 3RH, UK*
[10]*Department of Physics, Durham University, South Road, Durham, DH1 3LE, UK*
[11]*Astronomical Institute, Anton Pannekoek, University of Amsterdam, Science Park 904, NL-1098 XH Amsterdam, The Netherlands*

Accepted 2021 February 11. Received 2020 December 24; in original form 2020 November 10

ABSTRACT

We present the results regarding the analysis of the fast X-ray/infrared (IR) variability of the black hole transient MAXI J1535−571. The data studied in this work consist of two strictly simultaneous observations performed with *XMM–Newton* (X-rays: 0.7–10 keV), VLT/HAWK-I (K_s band, 2.2 μm) and VLT/VISIR (*M* and *PAH2_2* bands, 4.85 and 11.88 μm, respectively). The cross-correlation function between the X-ray and near-IR light curves shows a strong asymmetric anticorrelation dip at positive lags. We detect a near-IR QPO (2.5σ) at 2.07 ± 0.09 Hz simultaneously with an X-ray QPO at approximately the same frequency ($f_0 = 2.25 \pm 0.05$). From the cross-spectral analysis, a lag consistent with zero was measured between the two oscillations. We also measure a significant correlation between the average near-IR and mid-IR fluxes during the second night, but find no correlation on short time-scales. We discuss these results in terms of the two main scenarios for fast IR variability (hot inflow and jet powered by internal shocks). In both cases, our preliminary modelling suggests the presence of a misalignment between the disc and jet.

Key words: accretion, accretion discs – X-rays: binaries.

1 INTRODUCTION

Black hole low-mass X-ray binaries (BH LMXBs) have been historically studied mainly in X-rays, where, depending on the accretion regime, great part of the dissipated gravitational energy is radiated away by either a geometrically-thin, optically-thick accretion disc (Shakura & Sunyaev 1973) or a geometrically-thick, optically-thin inflow (Esin, McClintock & Narayan 1997; Poutanen, Krolik & Ryde 1997). However, multiwavelength studies have shown that bright (non-thermal) emission is also present at lower (from optical-UV down to radio) frequencies (see e.g. Fender et al. 2001; Corbel & Fender 2002; Hynes et al. 2003; Gandhi et al. 2011). This low-energy emission is usually interpreted in terms of synchrotron radiation from either a hot magnetized geometrically-thick, optically-thin inflow, or a compact collimated jet (Malzac, Merloni & Fabian 2004; Veledina, Poutanen & Vurm 2013a; Malzac 2014).

In the last 20 yr, the study of sub-second optical-infrared (O-IR) variable emission from BH LMXBs has improved significantly our understanding of these systems. The first sub-second observations in the optical band revealed a complex phenomenology (Kanbach et al. 2001; Hynes et al. 2003; Malzac et al. 2003; Malzac et al. 2004). In particular, the first cross-correlation function (CCF) of XTE J118+40 showed an intriguing anticorrelation at negative lags (corresponding to X-ray delays), also known as the 'precognition dip'. This phenomenon was then confirmed by optical/X-ray observations of Swift J1753.5−0127 (Durant et al. 2008). Multi-epoch observations of the latter source showed evidence for an evolution of the correlation, from the 1–2 s positive response at the outburst peak to the precognition dip structure in the tail (Hynes et al. 2009; Veledina et al. 2017). Due to the weak radio emission of this object (Soleri et al. 2010; Tomsick, Fuerst & Belloni 2015), the described behaviour was associated with the hot inflow. In particular, a detailed modelling of this source showed that the observed CCF could be reproduced by assuming that the optical emission originates from both reprocessed and synchrotron radiation coming from a hot, magnetized inflow, while the X-rays are generated from the Comptonization of the synchrotron radiation (Veledina, Poutanen & Vurm 2011).

Further fast O-IR photometry observations led to the discovery of a 0.1-s O-IR lag with respect to the X-ray variability (Gandhi

★ E-mail: f.m.vincentelli@soton.ac.uk

et al. 2008; Casella et al. 2010). This behaviour was attributed to the jet and was well reproduced by the so-called 'internal shock model' (Kobayashi, Piran & Sari 1997; Spada et al. 2001; Jamil, Fender & Kaiser 2010) when linking the shells' velocities to the variations observed in X-rays (Malzac 2013, 2014). This demonstrated that fluctuations from the inflow can also be transferred into the outflow and opened the possibility to put new constrains on the jet parameters (Casella et al. 2010; Kalamkar et al. 2016; Gandhi et al. 2017; Vincentelli et al. 2019). Further multiwavelength observations permitted to deeply characterize the O-IR variability and to study the physical processes that take place inside these outflow. For example, there is now growing evidence that the O-IR jet emitting region is extended and probably stratified (Vincentelli et al. 2018; Paice et al. 2019; Vincentelli & Casella 2019); moreover, Malzac et al. (2018) recently showed that Doppler boosting modulation can also lead to an anticorrelation with X-rays on long time-scales.

Another important feature that gave new insight to the geometry of these systems are the quasi-periodic oscillations (QPOs). These oscillations are very common in X-rays and have been attributed to Lense–Thirring precession of the hot inflow (Stella & Vietri 1998; Ingram & Done 2012; Motta et al. 2015), although this interpretation is still somewhat matter of debate (Ingram & Motta 2020; Ma et al. 2020; Marcel & Neilsen 2020; Marcel et al. 2020). At lower energies, similar and simultaneous QPOs in the optical band have been explained in terms of synchrotron radiation from a precessing magnetized inflow (Veledina, Poutanen & Ingram 2013b; Veledina et al. 2015). In GX 339−4, the first QPO observed in the IR band (Kalamkar et al. 2016) was found in harmonic relation with an X-ray QPO, similar to its optical counterpart found some years earlier (Motch et al. 1983). Both precessing hot inflow and the inflow plus jet can qualitatively account for this behaviour, but currently the quantitative agreement has been proved only for the latter alternative, using the internal shocks model (Malzac et al. 2018).

MAXI J1535−571 is an X-ray transient discovered by the Monitor of All-sky X-ray Image Gas Slit Camera on the International Space Station (Matsuoka et al. 2009) and by the Burst Alert Telescope on board of the *Neil Gehrels Swift Observatory* in 2017 September (Kennea et al. 2017; Negoro et al. 2017). From the first observations, it was noticed that the source displayed strong X-ray variability, including low-frequency QPOs (Gendreau et al. 2017; Mereminskiy & Grebenev 2017), and very bright radio emission with a flat radio spectrum (Russell et al. 2017). Strong emission in the IR was also observed (Dinçer 2017). This led to identify the source as a BH LMXB. During the outburst, despite being heavily absorbed (neutral column density $N_{\rm H} \approx 10^{22}$ cm^{-2}), the source reached extremely high flux levels, up to 5 Crab in the 2–20 keV band (Shidatsu et al. 2017).

An intensive multiwavelength campaign was rapidly coordinated to track the evolution of the source (Sivakoff 2017). Due to its position in the sky, only few observations could have been made with the Very Large Telescopes (VLTs) before the source became too low on the horizon. In this paper we present the results from two strictly simultaneous near-IR and X-ray observations, aimed at studying the fast multiwavelength variability of this source. We complement the study using also, for the first time, strictly simultaneous mid-IR observations. We find that the properties of fast near-IR variability put tight constraints on the current jet and accretion flow models.

2 OBSERVATIONS

Strictly simultaneous multiwavelength observations were taken during the nights of 2017 September 14 and 15 (MJD 58010–58011), while the source was in its hard-intermediate state (Baglio et al. 2018; Bhargava et al. 2019; Russell et al. 2019). Near- and mid-IR data were collected with HAWK-I and VLT Imager and Spectrometer for the mid-infrared (VISIR) respectively, both mounted at the ESO VLTs; X-rays data were collected with the EPIC-pn camera on board the ESA satellite *XMM–Newton* (see Fig. 1). The epochs of the observations are reported in Table 1.

2.1 X-ray data: *XMM–Newton*

X-ray data were collected with the EPIC-pn camera. Observations were taken in *Burst mode* (OBS ID: 0795712001 and 0795712101). The data reduction was carried out using the XMM Science Analysis System (SAS v15). In particular, the source counts were extracted in the range RAWX: 28–48 (corresponding to an angular size of ≈86 arcsec along RAWX). Due to the high absorption of the source, X-ray events were extracted only between 2 and 10 keV. The mean count rate of the two observations was found to be very similar: 234 ± 1 counts s^{-1} for the first night, and 226 ± 1 counts s^{-1} for the second. Data were then barycentred with the BARYCEN software and binned in a light curve of 5.7 ms.

2.2 Near-IR data: VLT/HAWK-I

Near-IR sub-second data were collected with HAWK-I (Pirard et al. 2004) mounted at the VLT UT-4/Yepun (Program: 099.D-0068(A)). 1-h-long observations were taken in the $K_{\rm s}$ band (effective wavelength 2.2 μm) with a time resolution of 0.125 s. Images were stacked in 'data cubes' of 250 frames, separated by a gap of ≈3 s. A fraction of the cubes was affected by frame-losses. For cross-correlation analysis, cubes with frame losses were therefore discarded in order to avoid to introduce spurious lags. During the observations (especially in the second part of the first night), the target ended up a few pixels from the edge of the detector, introducing spurious features in the light curve. To be conservative, we decided not to include the cubes affected by the described problem (hence the large gaps seen in Fig. 1).

The telescope was pointed to 15:35:41.6, −57:11:22.9 (RA, Dec.) at an angle of 70° in order to have the target on the lower left-hand quadrant (Q1) together with the reference star with a $K_{\rm s}$ magnitude of 11.55 ± 0.02. The data reduction was performed using the ULTRACAM data reduction software tools (Dhillon et al. 2007). Parameters for the reduction were derived from the bright reference star point spread function and position. To account for seeing and transmission variations, the ratio between the source and the bright reference star count rate was used. Individual power spectral densities (PSDs) of the non-variable reference and comparison star showed that the variability induced by the seeing is extremely low, as compared to the intrinsic variability of the target, and was successfully removed by taking the ratio between the target and the bright reference star. Using such extraction, we found an average $K_{\rm s}$ magnitude of 11.52 ± 0.01 (non-dereddened flux of ≈16 mJy) for both nights. This in good agreement with the near-IR data in Baglio et al. (2018) taken on the same nights by REM. The time of each frame was then put in the Dynamical Barycentric Time system.

2.3 Mid-IR data: VLT/VISIR

Mid-IR observations were obtained with VISIR (Lagage et al. 2004) mounted at the VLT-UT3 Melipal (Program 099.D-0884(A)). The instrument was set in small-field imaging mode, with a pixel scale of 45 mas pixel^{-1}, and the *M* and *PAH*2_2 filters were used on September 14 and 15, respectively (covering the 4.85−11.88 μm wavelength

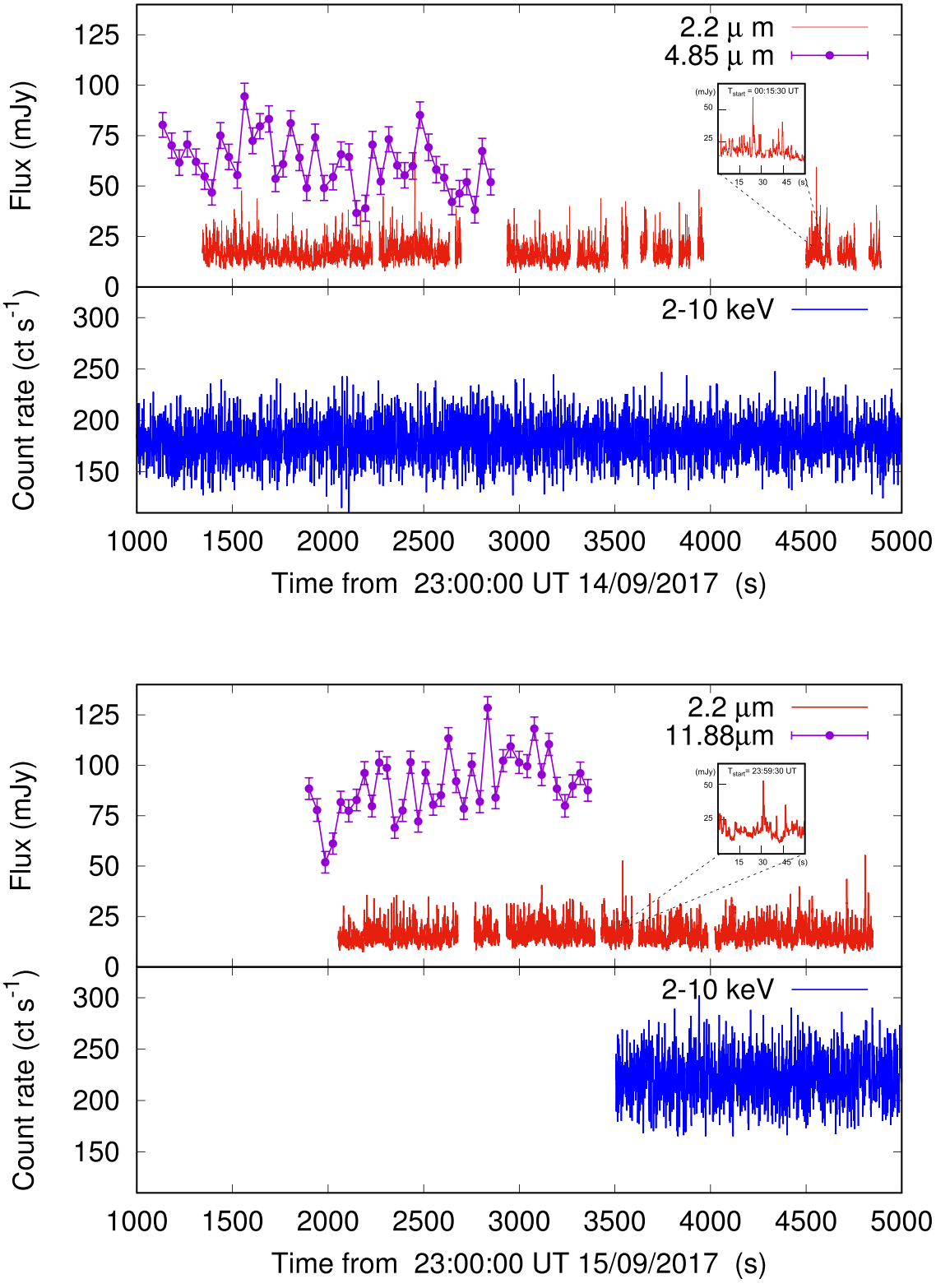

Figure 1. Light curves during X-ray / near- and mid- IR strictly simultaneous windows for the night of the 14th (top panel) and 15th (bottom panels) of September 2017 (N.B. X-ray observation for the 15th started around midnight, i.e. at ≈3600s; see Table 1). The plot shows the near- and mid-IR (red and purple, respectively) *observed* fluxes (not de-reddened) as a function of time. Blue curve shows the 2–10 keV count rate. While for the near- and mid- IR light curves we used the time resolution of the original data, the X-ray light curve was rebinned with resolution 1s.

Table 1. Summary of the multiwavelength campaign on the BH LMXB MAXI J1535−571 on 2017 September 14 and 15.

Night of the Start Time	Telescope/Instrument	Energy band	Start time (UT)	End time (UT)
	XMM–Newton/Epic-PN	0.5–10 keV	16:47:04	01:08:44
14/09	UT-4/HAWK-I	K_s (2.2 μm)	23:26:21	00:21:08
	UT-3/VISIR	M (4.85 μm)	23:19:22	23:46:20
	XMM–Newton/Epic-PN	0.5–10 keV	23:59:09	04:20:02
15/09	UT-4/HAWK-I	K_s (2.2 μm)	23:34:15	00:19:25
	UT-3/VISIR	*PAH*2_2 (11.88 μm)	23:29:54	23:53:26

range; see Table 1). Every observation consisted of 1000 s of time on source, characterized by 44 nodding cycles. In total, considering chopping and nodding between sky and source, the total exposure time was 1800–1900 s per observation.

Reduction of data was performed using the VISIR pipeline, available in GASGANO.[1] Sensitivities were estimated thanks to the observation of two standard stars (HD161096 and HD163376) on the same night and telescope configuration. After recombination of the chop/nod cycle raw images, aperture photometry was performed by means of an aperture that was large enough to avoid that possible seeing variations could affect the portion of the flux falling in the aperture. We note that the target of the observations was bright enough to allow a detection in individual observations. The VISIR pipeline requires that observations are combined in groups of multiples of two. In order to achieve a flux from each observation for this work, we therefore had to combine each image with the first observation on each night, then take into account the flux of this first observation to obtain the light curve. Using this method, we were able to sample the data twice as fast with respect to Baglio et al. (2018). In particular, each time bin has 27.8-s exposure, with a varying gap of ≈10 s between the bins due to the chop/nod cycle and read-out. Also in this case, the resulting light curve was then put in Dynamical Barycentric Time system.

No clear variability of the background was detected during the entire VISIR observations (see also Baglio et al. 2018 for details). A variation of (7–8) per cent in the ADU/flux conversion factor over different dates has instead been observed. This variability can however be caused by the different weather and sky conditions for different dates, as well as different air masses. Therefore, any possible mid-infrared variability of MAXI J1535−571 can be safely considered as intrinsic to the source.

3 DATA ANALYSIS

3.1 X-ray and near-IR power spectral densities

The properties of the X-ray and near-IR variability were studied through Fourier power spectral analysis. The X-ray and near-IR light curves were divided in 16 384-bin and 512-bin long segments, respectively. We computed the PSD of each segment in squared root mean square (rms) normalization (see e.g. Belloni & Hasinger 1990; Miyamoto et al. 1991; Vaughan et al. 2003) and then applied a logarithmic binning factor of 1.05 to the resulting average. The gaps between the cubes in the near-IR data were filled with simulated data, following the procedure described in Kalamkar et al. (2016). For the near-IR case, in order to reach lower frequencies without affecting the statistics of the higher frequencies, we also computed a PSD with the light curve rebinned to 10 s (much longer than the ≈3-s gaps) using 16 bins per segment.

Fig. 2 shows the PSDs for both epochs in X-rays and the in near-IR. The X-ray PSD does not change significantly between the two nights. In order to quantify the overall variability, a fit with multiple Lorentzian components was performed (Belloni, Psaltis & van der Klis 2002). Fig. 2 (bottom panels) shows how the broad-band noise can be well fitted by two Lorentzians centred at ≈0.5 and ≈5 Hz, respectively, while a type-C QPO (Casella, Belloni & Stella 2005; Motta et al. 2015) and its second harmonic are clearly detected at ≈2.25 and 4.5 Hz. These values are consistent with the values measured from quasi-simultaneous *Astrosat* X-ray timing observations (Bhargava et al. 2019; Sreehari et al. 2019). Results from the fit are reported in Table 2.

The near-IR PSDs show clear differences with respect to the X-rays: The low-frequency variability appears to dominate the IR PSDs, with a clear break at around 1 Hz, while the X-ray PSDs are dominated by variability in the 0.1–10 Hz frequency range. Similarly to the X-rays, we modelled the near-IR PSDs with a number of Lorentzian components. The broad-band noise, which in this case extends up to the Nyquist frequency, shows an excess at the highest frequencies, suggesting the presence of aliasing. Therefore, the fit was performed excluding frequencies above 3 Hz. During the first night, the broad-band noise was well described with three components, centred at 0 (fixed), ≈0.3, and ≈1 Hz: the latter one identifying the break visible in the PSD. During the second night, the centroid frequencies of the three components remained the same, although the high-frequency component narrowed significantly, and an additional fourth, even narrower component was (at ≈2.5σ level) required by the fit. The centroid frequency of this additional component is consistent with that of the QPO detected in the simultaneous X-ray light curve. In order to confirm this hypothesis, we fixed the frequency and width of this component to the one measured in the X-rays, leaving only the normalization as a free parameter. The amplitude of the QPO in this case was found significant at a 3σ level, strengthening the evidence for a QPO in the infrared band.

3.2 X-ray/near-IR cross-correlation analysis

The correlated variability between the X-ray and near-IR light curves was investigated using both time- and frequency-domain techniques. In order not to distort the results, we used only the original light curves (i.e. without filling the near-IR gaps) and excluding cubes affected by frame-losses. We computed the CCF (Edelson & Krolik 1988) for all the simultaneous observations using the procedure described in Gandhi et al. (2010). The computed CCFs in the two nights present a strong asymmetric dip at positive lags (positive lags correspond to near-IR lagging behind the X-rays), with a ≲1-s sharp drop and an ∼5-s shallower rise (Fig. 3).

We quantified the possible noise contribution to the observed CCF by simulating $N = 10^3$ couples of uncorrelated light curves with

[1] https://www.eso.org/sci/software/gasgano.html

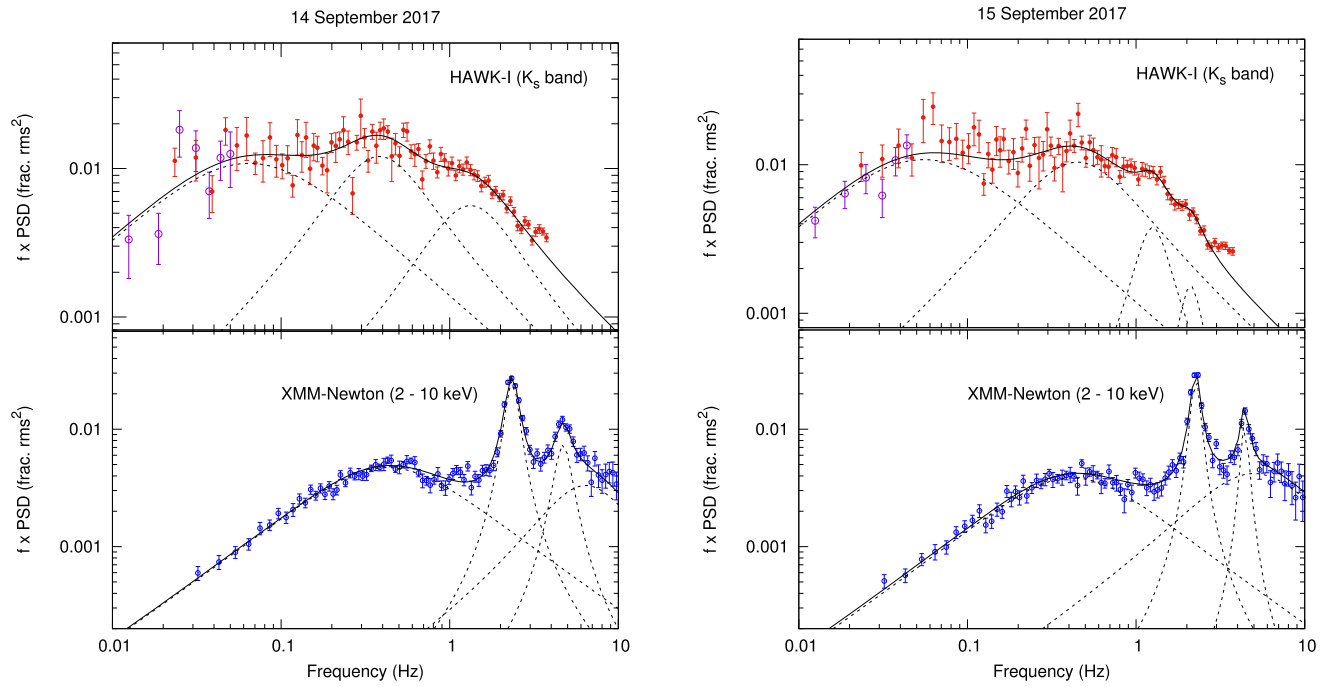

Figure 2. PSDs computed from the HAWK-I and *XMM–Newton* light curves for the nights of 2017 September 14 and 15. The models fitted to the PSDs and their individual components are shown with black and dashed lines, respectively. Data above 3 Hz are not used for fitting purposes due to clear aliasing contribution. Empty purple points represent the near-IR PSD computed with a 10-s light curve and 16 bins per segment.

Table 2. Parameters of the fit to the PSD with multiple Lorentzian components, $L(f) = A/[(f - f_0)^2 + (\Delta/2)^2]$.

Date	Band	Comp.	f_0 (Hz)	Δ (Hz)	A (10^{-3} Hz)	rms	Q	χ^2/dof
14/09	X-rays	1	0.12 ± 0.02	0.82 ± 0.02	13 ± 1	0.356 ± 0.001	0.14 ± 0.02	140/102
		2	2.33 ± 0.01	0.46 ± 0.02	7.9 ± 0.3	0.089 ± 0.004	2.8 ± 0.07	
		3	4.66 ± 0.05	1.2 ± 0.3	3 ± 1	0.05 ± 0.01	4 ± 1	
		4	5 ± 1	9 ± 1	5 ± 2	0.07 ± 0.02	0.6 ± 0.1	
15/09	X-rays	1	0.15 ± 0.03	0.78 ± 0.06	10 ± 1	0.08 ± 0.01	0.19 ± 0.04	101/102
		2	2.25 ± 0.05	0.31 ± 0.02	6.4 ± 0.3	0.08 ± 0.01	7.3 ± 0.5	
		3	4.4 ± 0.03	0.5 ± 0.1	1.8 ± 0.2	0.05 ± 0.01	9 ± 2	
		4	3 ± 1	9 ± 2	9 ± 2	0.08 ± 0.02	0.3 ± 0.1	
14/09	Near-IR	1	0 (fixed)	0.13 ± 0.02	3.4 ± 3	0.13 ± 0.02	–	83/80
		2	0.3 ± 0.04	0.51 ± 0.08	22 ± 5	0.14 ± 0.03	2.2 ± 0.1	
		3	1.1 ± 0.2	1.6 ± 0.2	9 ± 2	0.08 ± 0.02	0.7 ± 0.2	
15/09	Near-IR	1	0 (fixed)	0.11 ± 0.01	34 ± 3	0.13 ± 0.02	–	86/79
		2	0.28 ± 0.076	0.69 ± 0.12	22 ± 4	0.29 ± 0.02	0.4 ± 0.1	
		3	1.2 ± 0.1	0.6 ± 0.2	3 ± 1	0.05 ± 0.01	1.5 ± 0.6	
		4	2.07 ± 0.09	0.77 ± 0.25	0.8 ± 0.3	0.03 ± 0.01	3 ± 1	

Notes. We additionally define $Q = f_0/\Delta$. The fractional rms of each Lorentzian was obtained from the squared of the integration over the whole frequency range.

the same power-spectral properties of our data set. The resulting distribution of of the N uncorrelated CCFs has a standard deviation of 0.016 (grey-shaded area in Fig. 3). The anticorrelation dip appears statistically significant, while the peaks observed at lags larger than ±5 s – as well as those at negative lags – are consistent with noise.

To investigate further such correlated variability, Fourier cross-spectral analysis was applied. In particular, intrinsic coherence and lags were computed using the procedure described in Uttley et al. (2014) (see also Vaughan & Nowak 1997; Ingram 2019, and references therein). The presence of frames losses forced us to discard a significant fraction of the data cubes in the cross-correlation analysis. The remaining 'cleaned' light curve presented many interrupted segments, with gaps much longer than those seen between two consecutive data cubes (see Fig. 4). In order to compute the cross-spectral densities, we used 64-bin-long segments, which allowed us to explore frequencies down to 0.125 Hz. In order to probe longer time-scales, one would have to either deal with much lower statistics (because of the lower number of sufficiently long intervals) or fill the gaps between intervals. In the latter case, even though the resulting statistics can be formally high, the resulting cross-spectra

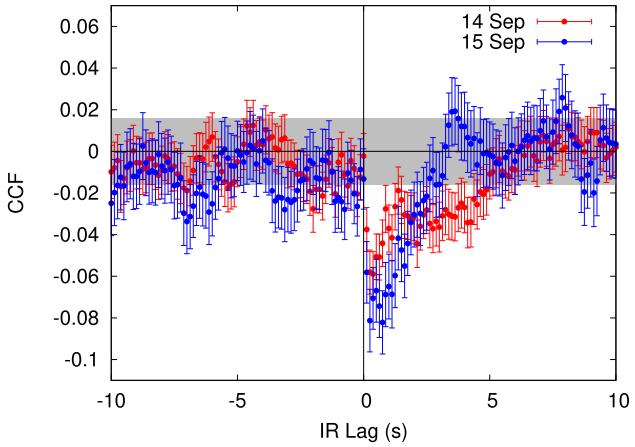

Figure 3. Near-IR/X-ray CCF computed using the *XMM–Newton*/Epic-PN (2–10 keV) and HAWK-I K_s light curves for the two nights of observations (September 14 and 15, red and blue, respectively). The 1σ confidence level is shown in grey. An anticorrelation dip at positive lags is clearly detected in both nights.

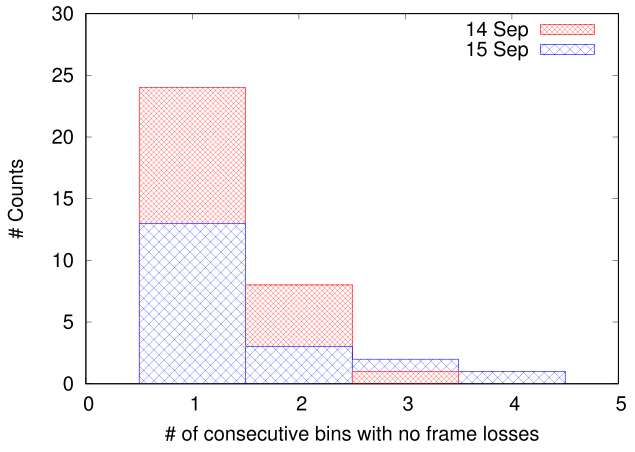

Figure 4. Histogram of the number of consecutive data cubes with no frame losses. For both nights, the majority of the segments of the cleaned light curve consisted of a single data cube. This means that the distance between the segments was (almost always) too large to be filled with standard methods (see also: Kalamkar et al. 2016).

would appear significantly distorted, as confirmed by simulations. However, given the width of the dip in the CCF, frequencies in the ≈0.1–0.25 Hz range are still expected to contribute to the observed anticorrelation. Therefore, our choice is still suitable for our purpose. Due to the low statistics, and given the similar timing properties during the two observations, cross-spectral analysis was performed combining the data from both nights together. We also checked the data for the individual nights but no significant variation from the described results was found. The results are shown in Fig. 5.

The intrinsic coherence of the two data sets is very low for almost all the probed frequencies. Nevertheless, the phase lags, though scattered, seem to show a clear trend. At low frequencies there is evidence for a (nearly) constant phase lag at $\sim -\pi/2$, while at frequencies higher than the QPO, the phase lags are unconstrained, thus oscillate between $-\pi$ and π. A somewhat higher coherence of 0.25 ± 0.1 (1σ error) is measured over the frequency range where the QPO is detected in the X-ray light curve. In this range, we also find the phase lag consistent with 0 ($\approx \pi/6$ rad, 3σ upper limit). We tested the significance of this variation by integrating the phase lags and coherence within the QPO frequencies (2.05–2.3 Hz) and in an equally large bin, centred just before the QPO (1.7–2.05 Hz). The phase lags pass from -0.8 ± 0.2 rad. outside the QPO, to 0.05 ± 0.1 rad (1σ); the coherence, instead, increases from 0.08 ± 0.02 to 0.12 ± 0.02 (1σ). This clearly shows the presence of an additional correlated component associated with the QPOs observed in both X-rays and IR at ≈2.1 Hz.

3.3 Correlations with mid-IR

The variability properties of the mid-IR light curve have already analysed by Baglio et al. (2018). During the first night (4.85 μm), the source showed a flux of 62.4 mJy and a fractional rms of 17.2 ± 8.4 per cent; during the second one (11.88 μm), a flux of 90.2 mJy and a 14.9 ± 4.8 per cent rms were measured. Here we focus on the correlated variability between mid-IR and the near-IR/X-ray light curves. While the correlation with the near-IR band could be computed for both nights, strictly simultaneous X-ray/mid-IR coverage was obtained only during the first night.

Similarly to the near-IR/X-ray case, we computed the CCF using 50-s time bins. Errors were estimated following the procedure described in Edelson & Krolik (1988) and Gandhi et al. (2010). We then evaluated the noise contribution by applying the same method described in Section 3.2. The CCFs are plotted in Fig. 6, with grey shades representing the 1σ, 2σ, and 3σ confidence levels. For the first night, we did not find any significant correlation between X-ray and mid-IR nor between near-IR and mid-IR light curves. A visual inspection of the light curves and the PSDs suggests that the reason behind this non-detection is the lack of variability for Fourier frequencies lower than ≈0.03 Hz (30-s time-scales).

The near-/mid-IR CCF of the second night instead presents two peaks at ≈3σ-level at 0 s and 100 s lags (mid-IR lags behind near-IR). We note, however, that during the second night, the mid-IR light curve shows a slowly increasing long-term trend, which could affect the CCF. We therefore computed the CCF after removing a linear trend to the light curve (see Fig. 6). The correlation in the second case is below 2σ (simulations showed that the confidence levels did not change significantly after the de-trending). This shows that the observed correlation is due to the long-term trend, and not originating from the fast time-scales variations. In order to visualize this better, we also plotted the mid-IR versus near-IR correlation diagram (Fig. 7), averaging the HAWK-I values within the 27.8-s VISIR exposures. The Pearson correlation coefficient between the two series is $\rho = 0.56$, which according to a simple t-distribution is significant at an ≈3σ level. We also quantified the relation between the near and the mid-IR variations by fitting as a power law $F_{\rm mid\text{-}IR} \propto F^{\beta}_{\rm near\text{-}IR}$, finding a slope of $\beta = 0.7 \pm 0.2$.

4 DISCUSSION

4.1 Power spectrum and QPO

We observe strongly variable near-IR emission from the BH LMXB MAXI J1535−571 in its intermediate state. The broad-band variability extends down to sub-second time-scales, albeit with a clear break in the PSD at ≈1 Hz. Similar behaviour has been reported already in a few BH LMXBs (Motch et al. 1983; Casella et al. 2010; Gandhi et al. 2010; Kalamkar et al. 2016; Veledina et al. 2017; Vincentelli et al. 2018). Superimposed on the strong broad-band noise, a ∼2.1-Hz QPO is simultaneously detected both in the X-rays and (marginally) in the near-IR PSDs, which we identify as a type-C QPO. It is interesting to notice that the Q factor of the (X-ray) main QPO and

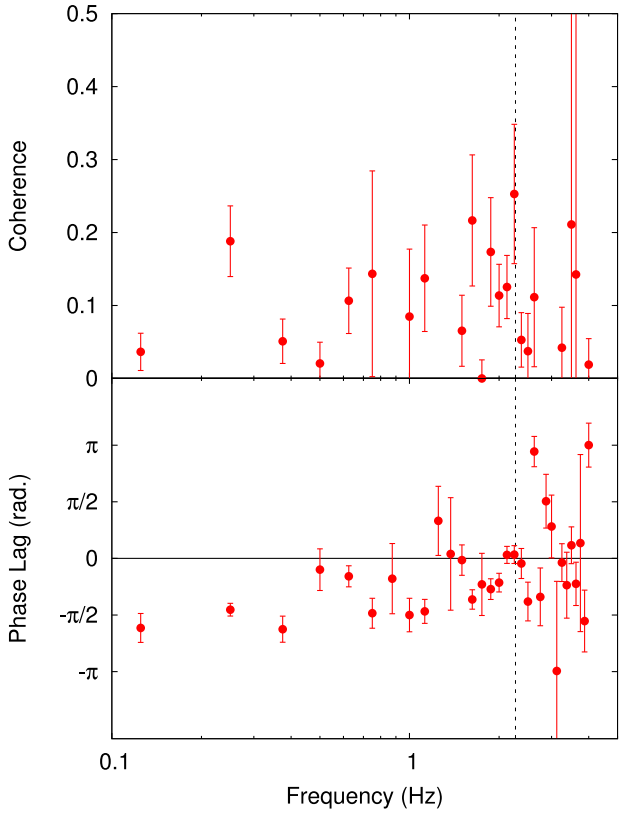

Figure 5. Intrinsic coherence (top panel) and phase lags (bottom panel) computed between near-IR and X-ray light curves, combining data from both nights. 64-bin segments were used. Vertical dashed line shows the position of the QPO.

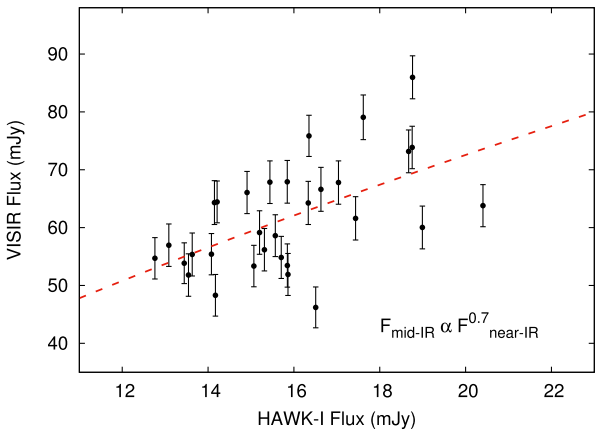

Figure 7. Mid-IR versus near-IR correlation diagram for the second night. As for Fig. 1, the fluxes are not de-reddened. A correlation of 3σ is detected.

its harmonic are consistent within the errors. This has already been observed in other sources (Rao et al. 2010; Ratti, Belloni & Motta 2012) and indicates that the origin of the quasi-periodicity is due to the fluctuations in the frequency rather than the amplitude. This was found to be consistent with the predictions of Lense–Thirring precession of the accretion flow (Ingram, Done & Fragile 2009; Ingram & Done 2012, see however also Marcel & Neilsen 2020).

O-IR type-C QPOs have been reported in a number of BH LMXBs so far (Motch et al. 1983; Gandhi et al. 2010; Veledina et al. 2015). In particular, GX 339-4 showed IR QPOs in harmonic relation with the X-ray one (Kalamkar et al. 2016), or without a clear equivalent in the X-ray PDS (i.e. X-ray QPO marginally or not detected Vincentelli et al. 2019). Despite being weaker compared to GX 339-4, (3 ± 1 per cent versus 6 ± 2 per cent, see tables 1 and 2 in Kalamkar et al. 2016), our IR QPO is the fastest detected to date (by almost a factor of 10); in addition (differently from Malzac et al. 2018), we also find a zero phase lag. Interestingly, optical/X-ray lags consistent with 0 at the QPO frequency have also been reported from the BH LMXB Swift J1753.0−0127 (Veledina et al. 2015), which might suggest a similar physical scenario.

The origin of similar fast-variable O-IR emission is still matter of debate (Poutanen, Veledina & Revnivtsev 2014; Uttley & Casella 2014). The two most promising scenarios invoke synchrotron radiation either from a magnetized hot accretion flow (Veledina et al. 2013a), or from a collimated jet (Malzac 2014). Using the obtained results of the simultaneous near-IR and X-ray QPOs, we can put constraints on both models.

In the hot flow scenario, the O-IR QPOs are related to the Lense–Thirring (LT) solid-body precession of the hot medium (Veledina

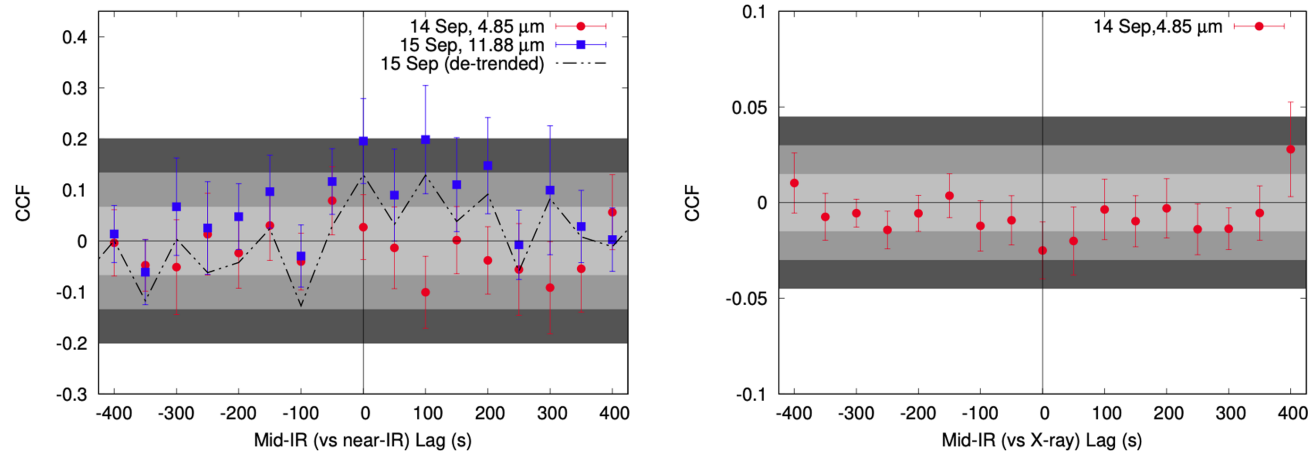

Figure 6. Mid-IR/near-IR (left-hand panel) and mid-IR/X-ray (right-hand panel) CCFs. 1σ, 2σ, and 3σ confidence levels are plotted with different grey shades. Dot–dashed line in the left-hand panel shows the CCF for the second night after the linear de-tremding was applied.

et al. 2013b). This model has been mainly tested with QPOs at much lower frequencies ($\approx 10^{-3}$–10^{-2} Hz; Veledina et al. 2017); however, as long as the oscillation is also detected in X-rays, there are no principle restrictions on the QPO frequency. If we assume that the observed near-IR frequency $\nu = 1.4 \times 10^{14}$ Hz is the frequency at which the synchrotron spectrum cuts off towards longer wavelengths (the so-called turnover frequency, Wardziński & Zdziarski 2001, see also equation (3) in Veledina et al. 2013a), it is possible to set a limit to the size of the partially absorbed synchrotron-emitting region. To comply with the required near-IR frequency, we obtain constraints on the electron Thomson optical depth (τ) of the power-law electrons in the hot flow $\sim 10^{-3}$–10^{-2}, and the magnetic field in the medium $\sim 10^{4}$–10^{5}G, which can be achieved at $R/R_{\rm g} \sim$ 30–50 (for the black hole mass of 10 solar masses). This estimate is to be compared to the outer radius of the precessing accretion flow, as inferred from the Fourier frequency of the QPO, $f = 2.1$ Hz. Using equation (43) of Fragile et al. (2007) for the QPO frequency and substituting the estimate for the inner disc radius from Lubow, Ogilvie & Pringle (2002) (see also equation 2 Ingram et al. 2009), we obtain that the required radii can be achieved for the spin parameter $a \gtrsim 0.8$, radial power-law dependence of the disc surface density $\Sigma \propto R^{-0.5}$ (typical for advection-dominated accretion flows; Narayan & Yi 1994) and $H/R \sim 1$. Hence, in order to explain the simultaneous near-IR and X-ray QPO within the hot flow model, we require high spin and high disc aspect ratio. The obtained zero phase lag between the X-ray and near-IR QPO can be explained by the solid-body precession of the hot flow, if the orbital inclination is $\gtrsim 50^{\circ}$ (Veledina et al. 2013b). The high spin and orbital inclination seems to be consistent with recent X-ray spectral measurements (Miller et al. 2018; Xu et al. 2018; Sreehari et al. 2019).

The alternative scenario that is usually invoked for O-IR QPOs is the LT precession of a relativistic jet together with the X-ray emitting hot inflow. Recent 3D GRMHD simulations have shown that the jet can precess along with the hot inflow (Liska et al. 2018). Moreover, Malzac et al. (2018) showed that the amplitude and the width of the IR QPO observed in GX 339−4 during its hard-intermediate state in 2010 (Kalamkar et al. 2016) could be reproduced by the precession of a jet, by assuming a partial breaking of the coherence of its oscillations, as also expected during LT precession. For instance, if $\Gamma\beta \approx 0.2$–0.5 (where Γ is the jet Lorentz factor and $\beta = \sqrt{1-\Gamma^{-2}}$ is the dimensionless jet velocity), a precession angle of $\approx 5^{\circ}$ would produce the required 3 per cent rms observed in the IR.

The observed zero phase lag then imposes constraints on the distance between the X-ray and near-IR emission sites. This can be used to constrain the maximum inclination of the jet, and to set a lower limit to its speed (β). By taking into account projection effects, the distance between the two emitting regions will be $R = \beta c \Delta t/(1 - \beta \cos i)$, where $\cos i$ is the cosine of jet inclination angle with respect to the line of sight, and Δt is the near-IR/X-ray time lag. By integrating the cross-spectrum on the frequencies where the phase lag is consistent with 0, we obtained a 3σ upper limit to the time lag of 0.04 s.

Simulations from the internal shocks model have shown that the peak of the near-IR emission region (R) can span, depending on the jet physical conditions, a range of values from $\approx 5 \times 10^{3}$ to $\approx 5 \times 10^{5} R_{\rm g}$ (Malzac 2014; Malzac et al. 2018). Given also the limits to the jet first acceleration zone imposed by Russell et al. (2020), we set a conservative value for R of $5 \times 10^{3} R_{\rm g}$, which leads to a required jet Lorentz factor of $\Gamma \gtrsim 1.7$ and a jet inclination $i \lesssim 40^{\circ}$. It is interesting to notice that this is in good agreement with radio observations of MAXI J1535−571 performed close to our campaign, which revealed a relativistic ejection with a reported inclination $\leq 45^{\circ}$ (Russell et al. 2019). Given that X-ray spectral measurements seem to indicate a highly inclined disc (Miller et al. 2018; Xu et al. 2018; Sreehari et al. 2019), this suggests the presence of a misalignment between the orbital spin and jet axis, which may cause the jet precession. Rapid changes of jet orientation on the sky, recently seen in V404 Cyg and Cir X-1 (see e.g Coriat et al. 2019; Miller-Jones et al. 2019), support the possibility for such precession.

We notice that a combination of the two scenarios is also possible. For instance, the stronger IR variability observed at lower frequencies may indicate the presence of a significant contribution from the jet (Veledina et al. 2011; Malzac et al. 2018). Therefore, the weak QPO signal measured in this data set could then be simply be reproduced by assuming a higher τ and B (i.e. smaller radii with higher density and magnetic energy density), as the IR band would be falling in the self-absorption regime. A detailed simulation is however necessary in order to disentangle the contribution from these two components and to better understand the observed differences with respect to GX 339−4.

4.2 Cross-correlation analysis

Our analysis reveals a clear connection between the X-ray and the IR bands. The CCF presents a significant asymmetric anticorrelation at positive lags, without any evidence of positive correlation. Anticorrelations between X-ray and O-IR variability have already been seen in other BH LMXBs. One of the the most notable cases is probably the optical/X-ray CCF of Swift J1753.5−0127, which showed a strong anticorrelation at negative lags and a positive correlation at positive lags (Durant et al. 2008; Veledina et al. 2017). Such behaviour was successfully reproduced by invoking a combination synchrotron self-Compton radiation of the hot flow and reprocessing from the outer disc (Veledina et al. 2011, 2013a). The CCF observed in MAXI J1535−571, instead, shows an anticorrelation at positive lags and no significant (above noise level) positive correlations. A roughly similar CCF showing an anticorrelation with a positive lag of ≈1–2 s (which included though also a positive correlated peak at ≈5 s) has also been observed in Swift J1753.5−0127 during the declining phase of the 2005 outburst (Hynes et al. 2009; Veledina et al. 2017) and has been reproduced by the hot flow model, by invoking a second source of X-ray photons (see fig. 5 in Veledina et al. 2017). It is interesting to notice that Swift J1753.5−0127, as for our observations, was in the hard-intermediate state when such anticorrelation was observed.

In the Fourier domain, we detect a roughly constant negative phase lags $-\pi/2$ below ∼1 Hz. Given the similar shape of the CCF, the expected phase lags from the hot-inflow model are in good agreement with this result. We notice, however, that similar negative phase lags have also been observed in the BH LMXB GX 339−4 and have been successfully explained with the internal shocks model (Malzac et al. 2018). According to this scenario such a behaviour is mainly due to the differential response of the shocks to the input (X-ray) fluctuations.[2] An impulse response function defined as the derivative of a function is known to give a phase lag of $\pi/2$ (see also Jenkins & Watts 1969; Malzac et al. 2004). Depending on the inclination and on the Lorentz factor of the jet, such an effect can become more or

[2]In the internal shocks model (Malzac 2014), the shell velocity is proportional to the X-ray fluctuations. The shocks occur because of the difference in velocity between the shells, which leads to a differential response.

less dominant, changing the phase lag (see figs 13 and 14 in Malzac et al. 2018).

Always in this context it is not clear why the 0.1-s infrared lag, usually associated with the jet scenario, is not present. From the simulations shown in Malzac et al. (2018), the lag is expected in all tested configurations, and should not depend on the jet Lorentz factor, nor on the inclination. However, in the internal shocks scenario the dependence of the IR variability on the X-rays fluctuation is highly non-linear and difficult to predict without detailed simulations. It is possible that the QPOs dominating the X-ray PSD for frequencies higher than ≈2 Hz prevent the detection of the 0.1-s lag. A similar situation was already found in GX 339−4 (Malzac et al. 2018) where the presence of a low-frequency QPO was thought to pollutes the $-\pi/2$ phase lag expected in internal shocks scenario. Another possibility is that the 0.1-s lag dominates the lag spectrum at higher frequencies than usually observed. Paice et al. (2019) showed that – at least In the case of MAXI J1820+070 – indeed the 0.1-s lag can be observed up to at least 5 Hz.

4.3 Mid-IR

We present for the first time the analysis of the correlated variability between simultaneous X-rays, near-, and mid-IR data. No significant correlation was detected during the first night, while during the second, one correlation was found at an ≈3σ level, dropping below 2σ once the long-term trend of the light curves is removed. Such a behaviour can be explained by the fact that both X-ray and near-IR PDS show a low-frequency break at ≈0.03 Hz (30-s time-scales). This means that on the time-scales probed by the mid-IR observation, both the near-IR and the X-ray light curves show a small amount of variability, hampering the possibility to detect any correlation.

A detailed discussion of the mid-IR observations of MAXI J1535−571 carried out during our campaign has been presented in Baglio et al. (2018). The authors reported significant mid-IR variability on time-scales of minutes that, given also the strong excess shown in the spectral energy distribution (SED), was interpreted in terms of synchrotron emission from a collimated jet. Contribution from the hot inflow at these wavelengths seems also be unlikely when considering the preliminary parameters obtained in the previous section. The same authors, instead, conclude that in the near-IR band there may be potential contribution from both jet and accretion disc (Baglio et al. 2018; Russell et al. 2020). We therefore discuss our results regarding the mid/near-IR connection according to these two possible scenarios:

Both mid-IR and near-IR from jet. Being part of the same physical component, a tight correlation should be present between the two bands, with possible delays of the order of few seconds (Malzac et al. 2018). We notice, however, that although we do not find correlation on time-scales of tens of seconds, this does not necessarily point against this scenario. As mentioned above, neither X-ray nor near-IR emission display strong variability on time-scales comparable with VISIR's time resolution: Thus, a low connection is somehow expected in this case. New detailed simulations that include the low-frequency end of the X-ray fluctuation PSD may help to quantitatively test this scenario with this data set.

Mid-IR jet, near-IR hot inflow. On short time-scales, the expected correlation strongly depends on the physical parameters of the system, which can affect the responses of the two components. The shape of the CCF may have a complex shape that is difficult to predict without proper modelling. Nevertheless, if the same input mass-accretion rate fluctuations travel through the hot-inflow (where it emits in the near-IR) and then in the jet (emitting in the mid-IR), a lag of the order of seconds is expected to appear. On longer time-scales, instead, the two bands should be correlated, according to the well-known strong inflow–outflow connection of these sources (see e.g. Gallo, Degenaar & van den Eijnden 2018, and references there in).

Given that both scenarios can reproduce the observed correlation on longer time-scales, a self-consistent modelling with both the components is necessary in order to actually quantify the contribution of hot-inflow and jet in the near-IR. More importantly, the two scenarios have strongly different predictions when probing (sub-) second time-scales, which could not be reached with the current data set. Thus, new higher time resolution observations will provide crucial physical information.

5 CONCLUSION

In this paper, we report the discovery of correlated X-ray/near-IR variability from the BH LMXB MAXI J1535−571, studied with two observations on two consecutive nights in 2017 September. We can summarize our results as follows:

(i) Power spectral analysis reveals the presence of complex broad-band noise down to sub-second time-scales in both X-ray and near-IR bands. No significant differences were found in the PSDs during the two consecutive nights of our campaign. A QPO at ≈2.1 Hz is found both in X-rays and in the near-IR. The face-value significance of the near-IR QPO is 2.5σ, but the fact that the measured lags at the QPO frequencies have relatively small uncertainties demonstrates the QPO is present in the near-IR light curve. This is the first unambiguous detection of a near-IR and X-ray QPO at the same frequency. The high QPO frequency and nearly zero phase lag (with $\pi/6$ radians 3σ upper limit) between the bands puts tight constraints on the models. We discuss the origin of the near-IR QPOs in terms of two specific scenarios: Lense–Thirring precession of the hot accretion flow (Veledina et al. 2013b) or the simultaneous precession of the jet and the inflow (Malzac et al. 2018). Both scenarios provide constraints that seem to confirm previous indications of a misalignment between the disc and the jet.

(ii) The cross-correlation function shows a puzzling asymmetric anticorrelation at positive lags. Such feature corresponds to nearly constant phase lags $\approx -\pi/2$ (X-rays lag behind the near-IR). Similar behaviour was observed in GX 339−4 and explained in that case in the context of the internal shocks model (Malzac et al. 2018; Vincentelli et al. 2019), but also during the hard-intermediate state of Swift 1753.5−0127, reproduced by the hot inflow model involving two X-ray continua (Veledina et al. 2017).

(iii) We performed the first correlated analysis of the variable mid-IR (4.85–11.88 μm) and near-IR (2.2 μm) emission from a BH LMXB. No significant correlation is found during the first night, because of the lack of variability of the near-IR lightcuve on time-scales probed by the VISIR observation. The flux–flux correlation diagram for the second night revealed instead a 3σ level correlation, likely associated with a clearly visible long-term trend in the mid-IR light curve. The trends can be associated with oscillations on time-scales much longer than the corresponding segment of the light curve. In our case, from the trend visible in the lower panel of Fig. 1, we can only say that the oscillation has a characteristic time-scale $\gg$1000 s.

Fast multiwavelength variability is revealing to be one of the most powerful tools to study the innermost regions around accreting stellar-mass BHs, allowing us to put constraints on the accretion geometry of these systems. The analysis of an increasing number

of data sets, together with the development of theoretical models, are starting to shed light also on the physical processes that take place inside the jet. In particular, the results found in our analysis will provide a solid test for the state-of-the-art models. New high time-resolution multiwavelength observations, especially at longer wavelengths (e.g. with *JWST*; Gardner et al. 2006), will help to address many remaining open questions on these objects.

ACKNOWLEDGEMENTS

The authors are extremely grateful to the VLT and *XMM–Newton* astronomers, who allowed us to successfully collect strictly simultaneous data from three different telescopes. The authors would like to thank the referee for the useful comments that significantly improved this paper. The discussion of this paper benefited from the meeting 'Looking at the disc-jet coupling from different angles' held at the International Space Science Institute in Bern, Switzerland. FMV acknowledges support from STFC under grant ST/R000638/1. This work was supported by the Programme National des Hautes Energies of CNRS/INSU with INP and IN2P3, co-funded by CEA and CNES. AV acknowledges the Academy of Finland grants 309308 and 321722.

DATA AVAILABILITY STATEMENT

X-ray data are accessible from the *XMM–Newton* online archive.[3] Data from HAWK-I and VISIR instead are publicly available on the ESO online archive.[4]

REFERENCES

Baglio M. C. et al., 2018, ApJ, 867, 114
Belloni T., Hasinger G., 1990, A&A, 227, L33
Belloni T., Psaltis D., van der Klis M., 2002, ApJ, 572, 392
Bhargava Y., Belloni T., Bhattacharya D., Misra R., 2019, MNRAS, 488, 720
Casella P. et al., 2010, MNRAS, 404, L21
Casella P., Belloni T., Stella L., 2005, ApJ, 629, 403
Corbel S., Fender R. P., 2002, ApJ, 573, L35
Coriat M., Fender R. P., Tasse C., Smirnov O., Tzioumis A. K., Broderick J. W., 2019, MNRAS, 484, 1672
Dhillon V. S. et al., 2007, MNRAS, 378, 825
Dinçer T., 2017, Astron. Telegram, 10716
Durant M., Gandhi P., Shahbaz T., Fabian A. P., Miller J., Dhillon V. S., Marsh T. R., 2008, ApJ, 682, L45
Edelson R. A., Krolik J. H., 1988, ApJ, 333, 646
Esin A. A., McClintock J. E., Narayan R., 1997, ApJ, 489, 865
Fender R. P., Hjellming R. M., Tilanus R. P. J., Pooley G. G., Deane J. R., Ogley R. N., Spencer R. E., 2001, MNRAS, 322, L23
Fragile P. C., Blaes O. M., Anninos P., Salmonson J. D., 2007, ApJ, 668, 417
Gallo E., Degenaar N., van den Eijnden J., 2018, MNRAS, 478, L132
Gandhi P. et al., 2008, MNRAS, 390, L29
Gandhi P. et al., 2010, MNRAS, 407, 2166
Gandhi P. et al., 2011, ApJ, 740, L13
Gandhi P. et al., 2017, Nat. Astron., 1, 859
Gardner J. P. et al., 2006, Space Sci. Rev., 123, 485
Gendreau K. et al., 2017, Astron. Telegram, 10768
Hynes R. I. et al., 2003, MNRAS, 345, 292
Hynes R. I., Brien K. O., Mullally F., Ashcraft T., 2009, MNRAS, 399, 281
Ingram A., 2019, MNRAS, 489, 3927
Ingram A., Done C., 2012, MNRAS, 419, 2369
Ingram A., Motta S., 2020, New Astron. Rev., 85, 101524
Ingram A., Done C., Fragile P. C., 2009, MNRAS, 397, L101
Jamil O., Fender R. P., Kaiser C. R., 2010, MNRAS, 401, 394
Jenkins G. M., Watts D. G., 1969, Spectral Analysis and Its Applications, Holden Day, London
Kalamkar M., Casella P., Uttley P., O'Brien K., Russell D., Maccarone T., van der Klis M., Vincentelli F., 2016, MNRAS, 460, 3284
Kanbach G., Straubmeier C., Spruit H. C., Belloni T., 2001, Nature, 414, 180
Kennea J. A., Evans P. A., Beardmore A. P., Krimm H. A., Romano P., Yamaoka K., Serino M., Negoro H., 2017, Astro. Telegram, 10700
Kobayashi S., Piran T., Sari R., 1997, ApJ, 490, 92
Lagage P. O. et al., 2004, The Messenger, 117, 12
Liska M., Hesp C., Tchekhovskoy A., Ingram A., van der Klis M., Markoff S., 2018, MNRAS, 474, L81
Lubow S. H., Ogilvie G. I., Pringle J. E., 2002, MNRAS, 337, 706
Ma X. et al., 2020, Nat. Astron., 5, 94
Malzac J. et al., 2018, MNRAS, 480, 2054
Malzac J., 2013, MNRAS, 429, L20
Malzac J., 2014, MNRAS, 443, 299
Malzac J., Belloni T., Spruit H. C., Kanbach G., 2003, A&A, 407, 335
Malzac J., Merloni A., Fabian A. C., 2004, MNRAS, 351, 253
Marcel G. et al., 2020, A&A, 640, A18
Marcel G., Neilsen J., 2020, ApJ, 906, 6
Matsuoka M. et al., 2009, PASJ, 61, 999
Mereminskiy I. A., Grebenev S. A., 2017, Astron. Telegram, 10734
Miller J. M. et al., 2018, ApJ, 860, L28
Miller-Jones J. C. A. et al., 2019, Nature, 569, 374
Miyamoto S., Kimura K., Kitamoto S., Dotani T., Ebisawa K., 1991, ApJ, 383, 784
Motch C., Ricketts M. J., Page C. G., Ilovaisky S. A., Chevalier C., 1983, A&A, 119, 171
Motta S. E., Casella P., Henze M., Muñoz-Darias T., Sanna A., Fender R., Belloni T., 2015, MNRAS, 447, 2059
Narayan R., Yi I., 1994, ApJ, 428, L13
Negoro H. et al., 2017, Astron. Telegram, 10699
Paice J. A. et al., 2019, MNRAS, 490, L62
Pirard J.-F. et al., 2004, in Moorwood A. F. M., Masanori I., eds, Ground-based Instrumentation for Astronomy, Proc. SPIE, Vol. 5492, p. 1763
Poutanen J., Krolik J. H., Ryde F., 1997, MNRAS, 292, L21
Poutanen J., Veledina A., Revnivtsev M. G., 2014, MNRAS, 445, 3987
Rao F., Belloni T., Stella L., Zhang S. N., Li T., 2010, ApJ, 714, 1065
Ratti E. M., Belloni T. M., Motta S. E., 2012, MNRAS, 423, 694
Russell T. D. et al., 2019, ApJ, 883, 198
Russell T. D. et al., 2020, MNRAS, 498, 5772
Russell T. D., Miller-Jones J. C. A., Sivakoff G. R., Tetarenko A. J., Jacpot Xrb Collaboration, 2017, Astron. Telegram, 10711
Shakura N. I., Sunyaev R. A., 1973, A&A, 24, 337
Shidatsu M. et al., 2017, Astron. Telegram, 10761, 1
Sivakoff G. R., 2017, Astron. Telegram, 10714
Soleri P. et al., 2010, MNRAS, 406, 1471
Spada M., Ghisellini G., Lazzati D., Celotti A., 2001, MNRAS, 325, 1559
Sreehari H., Ravishankar B. T., Iyer N., Agrawal V. K., Katoch T. B., Mandal S., Nand i A., 2019, MNRAS, 487, 928
Stella L., Vietri M., 1998, ApJ, 492, L59
Tomsick J. A., Fuerst F., Belloni T., 2015, Astron. Telegram, 7962
Uttley P., Casella P., 2014, Space Sci. Rev., 183, 453
Uttley P., Cackett E. M., Fabian A. C., Kara E., Wilkins D. R., 2014, A&AR, 22, 72
Vaughan B. A., Nowak M. A., 1997, ApJ, 474, L43

[3] http://nxsa.esac.esa.int/nxsa-web/search
[4] http://archive.eso.org/eso/eso_archive_main.html

Vaughan S., Edelson R., Warwick R. S., Uttley P., 2003, MNRAS, 345, 1271
Veledina A., Poutanen J., Vurm I., 2011, ApJ, 737, L17
Veledina A., Poutanen J., Vurm I., 2013a, MNRAS, 430, 3196
Veledina A., Poutanen J., Ingram A., 2013b, ApJ, 778, 165
Veledina A., Revnivtsev M. G., Durant M., Gandhi P., Poutanen J., 2015, MNRAS, 454, 2855
Veledina A., Gandhi P., Hynes R., Kajava J. J. E., Tsygankov S. S., Revnivtsev M. G., Durant M., Poutanen J., 2017, MNRAS, 470, 48
Vincentelli F. M. et al., 2018, MNRAS, 477, 4524
Vincentelli F. M. et al., 2019, ApJ, 887, L19
Vincentelli F. M., Casella P., 2019, Astron. Nachr., 340, 319
Wardziński G., Zdziarski A. A., 2001, MNRAS, 325, 963
Xu Y. et al., 2018, ApJ, 852, L34

This paper has been typeset from a TEX/LATEX file prepared by the author.